Infrared Stokes imaging polarimeter using microbolometers

Michael W. Kudenov[1], J. Larry Pezzaniti[2], Eustace L. Dereniak[1], Grant R. Gerhart[3]

[1]The University of Arizona, College of Optical Sciences, 1630 E. University Blvd., Tucson, AZ
[2]Polaris Sensor Technologies, 200 West Court Sq. Suite 320, Huntsville, AL 35801
[3]U.S. Army TARDEC/RDECOM, AMSRD-TAR/MS 263, Warren, MI 48397-5000

ABSTRACT

A long wave infrared (LWIR) division of amplitude imaging Stokes polarimeter is presented. For the first time, to our knowledge, application of microbolometer focal plane array (FPA) technology to polarimetry is demonstrated. The sensor utilizes a wire-grid beamsplitter with imaging systems positioned at each output to analyze two orthogonal linear polarization states simultaneously. Combined with a form birefringent wave plate, the system is capable of snapshot imaging polarimetry in any one Stokes parameter (S_1, S_2 or S_3). Radiometric and polarimetric calibration procedures for the instrument are provided and data from the instrument are presented, demonstrating the ability to measure intensity variations corresponding to polarized emission in natural environments. As such, emission polarimetry can be exploited at significantly reduced cost, sensor size and power consumption over instruments based on more costly Mercury-Cadmium Telluride (MCT) FPA's.

Keywords: Infrared, Stokes, polarimetry, emission, polarization, microbolometer, form-birefringence.

1. INTRODUCTION

Stokes imaging polarimetry in the thermal infrared is of great interest in remote sensing for increasing the signal-to-clutter ratio between manmade objects and the natural environment [1]. A Stokes imaging polarimeter is capable of obtaining either the partial or complete polarization state of a scene via four Stokes parameters. These parameters express the state of polarization in a 4x1 matrix, defined as,

$$\mathbf{S}(x,y)=\begin{bmatrix} S_0(x,y) \\ S_1(x,y) \\ S_2(x,y) \\ S_3(x,y) \end{bmatrix}=\begin{bmatrix} I_0(x,y)+I_{90}(x,y) \\ I_0(x,y)-I_{90}(x,y) \\ I_{45}(x,y)-I_{135}(x,y) \\ I_R(x,y)-I_L(x,y) \end{bmatrix} \tag{1}$$

where x, y are spatial coordinates in the scene, S_0 is the total energy of the beam, S_1 denotes preference for linear 0º over 90º, S_2 for linear 45º over 135º, and S_3 for circular right over left polarization states. Each is defined by an addition or subtraction of intensity measurements that represent different analyzer states, and complete characterization requires at least four such states be measured. These measurements can be acquired over time by use of a rotating element (division of time) with a single imaging lens and Mercury Cadmium Telluride (MCT) focal plane array (FPA). Such an implementation yields a compact and relatively inexpensive instrument. However, it is susceptible to misregistration errors caused by platform or scene motion.

In many applications, Stokes parameters are acquired from moving platforms. To remedy concerns regarding temporal misregistration, the instrument must acquire multiple analyzer measurements in parallel. This requires a sensor design that exploits one of following three techniques: division of amplitude (DoAM), division of aperture (DoA), or division of FPA (DoF). In DoAM, multiple lenses, beamsplitters, polarization beamsplitters, and FPA's are utilized. The beamsplitters divide the pupil into orthogonal polarization states and the Stokes parameters are measured independently by separate lenses and FPA's. Alternatively, in DoA, the aperture of the optical system is replicated into four quadrants, each with a different analyzer. These four quadrants are then re-imaged onto a single FPA. Implementation of this technique requires relatively sophisticated optics to generate and re-image the four beams. Conversely, in DoF, a 2x2 region of pixels on the FPA is divided into a "super-pixel". On top of each pixel within the super-pixel are four different

Infrared Systems and Photoelectronic Technology IV,
edited by Eustace L. Dereniak, John P. Hartke, Paul D. LeVan, Randolph E. Longshore, Ashok K. Sood,
Proc. of SPIE Vol. 7419, 741908 · © 2009 SPIE · CCC code: 0277-786X/09/$18 · doi: 10.1117/12.828047

analyzers, typically consisting of wire grid polarizers oriented at 0º, 45º, 90º and 135º. Since the polarization analyzers are inherent to the FPA, standard off-the-shelf imaging lenses can be used for the optical system.

Compared to a division of time (DoT) approach, the DoAM or DoA techniques in the infrared can be cost prohibitive due to their large quantity of optical components (FPA's, lenses, beamsplitters, etc.). Consequently, the typical infrared polarimeter consists of a DoF approach on a MCT FPA. This yields parallel measurement of four analyzer states for determination of three Stokes parameters (S_0, S_1 and S_2) with one lens and FPA, yielding a more cost effective and compact sensor as compared to the DoAM or DoA approaches. But even a single pixilated MCT array can be prohibitively expensive for applications that might otherwise find utility from a sensor able to detect polarized emission.

Recent advances in microbolometer technology have enabled noise equivalent temperatures (NET) to approach that of systems equipped with MCT arrays (NET ~ 50 mK). As a result, we are able to demonstrate the effective implementation of microbolometer technology in a long wave infrared (LWIR) division of amplitude polarimeter. This is significant, since microbolometer FPA's are nominally one to two orders of magnitude less expensive than equivalent resolution MCT arrays; this makes emission polarimetry more accessible for use and study by a wider audience. Furthermore, microbolometers are compact and typically uncooled, making them smaller and more power efficient when compared to similar closed cycle MCT imaging systems. In this paper, we introduce details regarding the sensor configuration in section 2 and describe the polarimeter's radiometric and polarimetric calibration in section 3. Finally, indoor and outdoor data from the instrument are provided in section 4.

2. SENSOR CONFIGURATION

The LWIR two-camera imaging Stokes polarimeter takes two simultaneous intensity images of a scene for the calculation of one Stokes parameter [2]. This concept is nothing new; it has been implemented in the visible spectrum per Ref. [3]. However, its cost effective implementation in the LWIR has not been feasible until recently. A schematic of the two-camera polarimeter is depicted in Fig. 1.

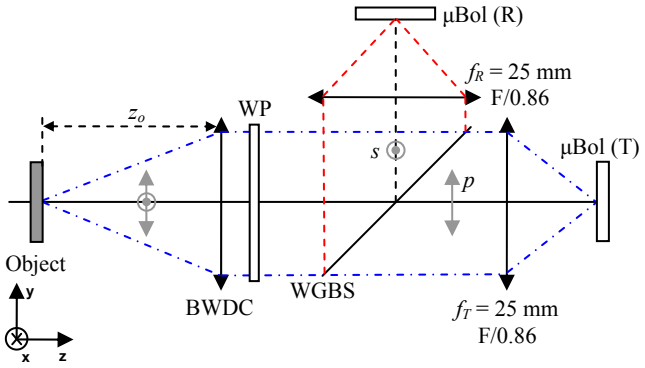

Fig. 1. System schematic for the two-camera microbolometer Stokes polarimeter. The BWDC is followed by the WGBS where the *s* and *p* polarization states are reflected (R) and transmitted (T), respectively, into one of two optical subsystems. The WGBS is oriented such that the reflection (*s*-polarization) and transmission (*p*-polarization) axes are oriented at 0º and 90º, respectively. The WP can be manually inserted into the optical path behind the BWDC for measurements of circular polarization states.

Spectral sensitivity of the sensor spans 7.5-13 µm and consists of two optical subsystems, each containing a lens and microbolometer (µBol). Each microbolometer is a model Photon 320 manufactured by FLIR Systems and contains 38x38 µm pixels with 324x255 spatial resolution elements. Both microbolometers are equipped with a 25 mm focal length, F/0.86 imaging lens that provides a +/- 13° field of view. In order to simultaneously focus both of these optical subsystems an additional lens is included and is referred to as a back working distance compensator (BWDC). This optic enables focus for object distances (z_o) of 1 m to infinity. Additionally, a form birefringent wave plate (WP) can be manually inserted or withdrawn from the optical path to enable the measurement of circular polarization. The WP has a spectrally band-averaged retardance of 85.8º. Lastly, the wire grid beamsplitter (WGBS) consists of aluminum wires deposited on Germanium substrate. The wires are anti-reflection (AR) coated with a known coating while the face

opposite the wires contains a proprietary coating optimized for 8-12 μm. This provides spectrally band-averaged reflected extinction ratios of 10 and transmitted extinction ratios greater than 30. A photograph of the partially and fully assembled polarimeter is portrayed in Fig. 2 (a) and (b), respectively.

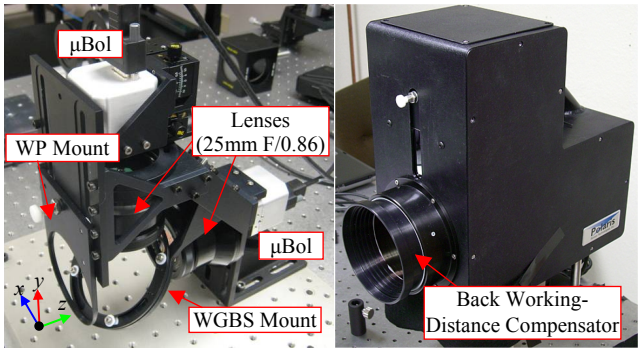

(a) (b)

Fig. 2. (a) Internal system of the two-camera microbolometer Stokes polarimeter. (b) Fully assembled instrument on the bench-top.

In order to perform the various measurements corresponding to S_1, S_2, and S_3, the analyzers must be altered. For S_1, the WGBS is oriented with its reflection axis at 0° and transmission axis at 90°, providing a measurement of the horizontal and vertical intensities I_H and I_V, respectively. For S_2, the WGBS is rotated by -45°, providing measurements of I_{135} and I_{45} in reflection and transmission, respectively. Lastly, for S_3, the WGBS is oriented identically to the S_1 configuration, but a form-birefringent wave plate (WP), oriented at 45°, is inserted into the optical path behind the BWDC. If the WP has a retardance of 90°, then measurements of I_R and I_L are obtained. However, since the retardance of the WP is actually 85.8º, uncertainty is contributed to the measurement of I_R and I_L at spatial locations where S_1 is present. The error, ε, depends on the ratio of S_1 to S_3,

$$\varepsilon = \sin(\delta) - \frac{S_1}{S_3}\cos(\delta) - 1 \tag{2}$$

where δ is the retardance of the WP. Since the S_3 signal is small in the LWIR, S_3 measurements are generally taken time-sequentially, with S_1 and S_2, to mitigate this error.

3. CALIBRATION

There are two processes that must be accomplished for instrument calibration. First, a radiometric calibration must be preformed such that all the pixels in both FPA's report identical outputs given identical inputs. Second a polarimetric calibration, which focuses on characterizing the system's measurement matrix, **W**, must be performed. Inversion of **W** yields a data reduction matrix that enables calculation of the input Stokes parameters at each spatial location within the scene.

3.1 Radiometric calibration

In order to produce reliable polarimetric data, the digital number (DN) from the detector must be converted to a radiometric quantity. A linear detector's digital output can be expressed as,

$$DN(m,n) = R(m,n)\Phi(m,n) + Off(m,n) \tag{3}$$

where m, n are the integer pixel coordinates, R is the pixel responsivity, Φ is the photon flux, and Off is the offset [4]. For radiometric calibration of the sensor, all pixels' responsivities and offsets must be calculated [5, 6].

To achieve this, a flat area black body, with dimensions 120x120 mm, is placed close to the front objective of the system so that it fills the entrance pupil. The temperature (T_{bb}) of the black body is changed to various known values and a linear function is fitted for each pixel output versus the incident irradiance on the FPA (approximately proportional to T_{bb}^4 per

Stefan-Boltzmann). Extrapolation of the fitted function to an input temperature of 0 K yields *Off* while the slope of the line indicates the responsivity *R*. Fig. 3 illustrates the linearity of the microbolometer by depicting the raw data for the center pixel in *DN* alongside the fitted line as a function of T_{bb}^4. All pixels will yield the same output at each of the input temperatures by inverse mapping; e.g. converting *DN* to T_{bb}^4, which is directly proportional to the incident irradiance.

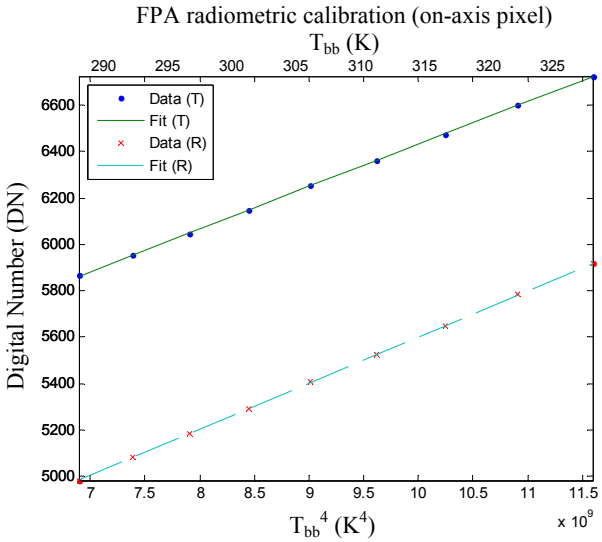

Fig. 3. FPA output and its corresponding fitted line for each microbolometer. The temperature (T_{bb}) of the black body was varied from 15 ºC (288 K) to 55 ºC (328 K) in 5 ºC increments.

3.2 Polarimetric calibration

As mentioned previously, the goal of the polarimetric calibration is characterization of the system's measurement matrix **W**. This is consistent with the matrix approach for calibration,

$$\mathbf{P}_{m,n} = \mathbf{W}_{m,n}\mathbf{S}_{m,n} \tag{4}$$

where $\mathbf{P}_{m,n}$ is a matrix of intensity measurements, $\mathbf{W}_{m,n}$ is the measurement matrix, and $\mathbf{S}_{m,n}$ is the incident Stokes vector [7]. Using the pseudoinverse of **W**, the Stokes vector can be calculated by,

$$\mathbf{S}_{m,n} = \mathbf{W}_{m,n}^{-1}\mathbf{P}_{m,n} \tag{5}$$

where $\mathbf{W}_{m,n}^{-1}$ is the system's data reduction matrix.

To characterize **W**, the instrument's analyzing elements (i.e. the WGBS, WP, etc.) are setup in a series of Mueller matrices with various free parameters (e.g. an element's orientation, retardance, etc.). Known polarization states are input into the instrument over the entire field of view (FOV) by use of a polarization generator. The theoretical output at each pixel is then fit, in a least squares fashion, to the measured output using the free parameters in the Mueller matrices.

3.3 Mueller matrix formalism

Propagation of the polarization state through an optical system via Stokes vectors is accomplished by representing each optical element by its Mueller matrix. In order to fully characterize the system's polarimetric response, and therefore calibrate its output, polarization attributes of the optical elements must be measured and their Mueller matrices calculated. A general Mueller matrix contains 4x4 elements,

$$\mathbf{M} = \begin{bmatrix} m_{00} & m_{01} & m_{02} & m_{03} \\ m_{10} & m_{11} & m_{12} & m_{13} \\ m_{20} & m_{21} & m_{22} & m_{23} \\ m_{30} & m_{31} & m_{32} & m_{33} \end{bmatrix} \tag{6}$$

There are two fundamental Mueller matrices that can be used to express an optical element's polarization interaction. The first is a diattenuator, which can be expressed in general as,

$$\mathbf{M}_D\left(T_x,T_y,\theta\right)=\frac{1}{2}\mathbf{R}\left(-\theta\right)\begin{bmatrix}\left(T_x+T_y\right) & \left(T_x-T_y\right) & 0 & 0\\ \left(T_x-T_y\right) & \left(T_x+T_y\right) & 0 & 0\\ 0 & 0 & 2\sqrt{T_xT_y} & 0\\ 0 & 0 & 0 & 2\sqrt{T_xT_y}\end{bmatrix}\mathbf{R}\left(\theta\right) \tag{7}$$

where T_x, T_y are the transmission ratios in the x and y directions, θ is the angle at which the diattenuator is oriented (as measured from the x-axis), and $\mathbf{R}(\theta)$ is the Mueller rotation matrix,

$$\mathbf{R}\left(\theta\right)=\begin{bmatrix}1 & 0 & 0 & 0\\ 0 & \cos\left(2\theta\right) & \sin\left(2\theta\right) & 0\\ 0 & -\sin\left(2\theta\right) & \cos\left(2\theta\right) & 0\\ 0 & 0 & 0 & 1\end{bmatrix} \tag{8}$$

The diattenuation matrix can be re-expressed as a function of the diattenuation coefficient (D), after normalization to ($T_x + T_y$),

$$\mathbf{M}_D\left(D,E,\theta\right)=\frac{1}{2}\mathbf{R}\left(-\theta\right)\begin{bmatrix}1 & D & 0 & 0\\ D & 1 & 0 & 0\\ 0 & 0 & 2E & 0\\ 0 & 0 & 0 & 2E\end{bmatrix}\mathbf{R}\left(\theta\right) \tag{9}$$

where D and E are defined as,

$$D=\frac{\left(T_x-T_y\right)}{\left(T_x+T_y\right)},\qquad E=\frac{\sqrt{T_xT_y}}{\left(T_x+T_y\right)} \tag{10}$$

and ($T_x + T_y$) is removed as a multiplying factor of Eq. 9, implying normalization of the analyzer vector to the m_{00} component, or similarly to the S_0 component of the output Stokes vector. Secondly is a retarder, which can be generally expressed by,

$$\mathbf{M}_R\left(\delta,\theta\right)=\mathbf{R}\left(-\theta\right)\begin{bmatrix}1 & 0 & 0 & 0\\ 0 & 1 & 0 & 0\\ 0 & 0 & \cos\delta & -\sin\delta\\ 0 & 0 & \sin\delta & \cos\delta\end{bmatrix}\mathbf{R}\left(\theta\right) \tag{11}$$

where δ is the retardance induced by the element, and is a measure of the relative phase delay between the eigenvectors of $\mathbf{M}_R$. An analyzer vector ($\mathbf{A}$) is given by the first row of the Mueller matrix,

$$\mathbf{A}=\begin{bmatrix}m_{00} & m_{01} & m_{02} & m_{03}\end{bmatrix} \tag{12}$$

The measurement matrix is composed of the analyzer vectors for each analyzer configuration,

$$\mathbf{W}=\begin{bmatrix}\mathbf{A}_1\\ \mathbf{A}_2\\ \vdots\\ \mathbf{A}_N\end{bmatrix}=\begin{bmatrix}m_{00,1} & m_{01,1} & m_{02,1} & m_{03,1}\\ m_{00,2} & m_{01,2} & m_{02,2} & m_{03,2}\\ \vdots & \vdots & \vdots & \vdots\\ m_{00,N} & m_{01,N} & m_{02,N} & m_{03,N}\end{bmatrix} \tag{13}$$

This implies a detector that is only sensitive to S_0, which is a valid assumption for a microbolometer [8].

3.4 Experimental polarimeter calibration setup

To create the input states for calibration, a polarization generator (PG) with well-known characteristics is placed in front of the instrument. The calibration setup is presented in Fig. 4. In the calibration system a black body is viewed in transmission (BB_1) and reflection (BB_2) via the PG. A sequence of measurements is made by rotating the PG through several angles (θ_G) at two different transmission black body temperatures. Taking the difference between these two measurements removes PG emissions and reflections, as well as offsets associated with emission from the internal components of the polarimeter. Fitting the Mueller matrix parameters can then be achieved on these data [6].

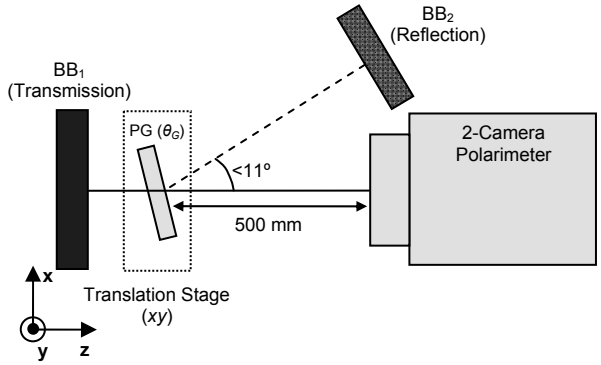

Fig. 4. Calibration setup for the two-camera polarimeter. A black body (BB_1) is viewed in transmission through the PG and another (BB_2) in reflection off the PG.

A concern regarding calibration is the large FOV of the sensor, which exceeds the aperture of the calibration optics. In order to calibrate all the pixels on the FPA simultaneously, the PG's polarization elements need to have a clear aperture (CA) on the order of 100 mm in diameter. Since cost effective calibration polarizers and retarders of this size are not readily available in the LWIR, the FOV was sampled discretely. This was accomplished by mounting the PG, which has a CA = 25 mm, on a translation stage. The stage was then moved to place the PG in various field positions within a 3x3 grid. Once the measurement matrix is calculated for the pixels at each of the 9 field positions, the pixels outside of these locations have their matrix components calculated via a cubic interpolation algorithm in Matlab.

3.5 Polarization generator characterization

Since precise knowledge of the PG determines the final accuracy of the calibration, its characterization must be thorough. In order to characterize both diattenuation and retardance within the polarimeter, both circular and linear polarization states must be used in the calibration procedure. To achieve this, two PG configurations were used. The first consisted of a rotating linear polarizer (LP) while the second contained a linear polarizer followed by a rotating form-birefringent WP. The WP has an unknown retardance δ_{WP} at a known angle θ_{WP}. Additionally, the WP has diattenuation inherent to the form-birefringent grating structure [9]. This can be simulated using the Mueller matrix for a general diattenuator oriented at θ_{WP} with diattenuation D_{WP} and $E_{WP} = 0.5$ ($D_{WP} < 0.1$). The Mueller matrix for the PG becomes,

$$\mathbf{M}_{PG} = \mathbf{M}_R\left(\delta_{WP}, \theta_{WP}\right)\mathbf{M}_D\left(D_{WP}, 0.5, \theta_{WP}\right)\mathbf{M}_D\left(0.98, 0.10, 90°\right) \tag{14}$$

Rotation of the WP from 0º to 360º in 20º increments is performed for both low and high transmission black body (BB_1) temperatures of 313 K and 373 K, respectively. The reflection black body (BB_2) temperature is constant at 308 K. As discussed previously, subtraction of the low temperature from the high temperature measurements removes radiometric offsets. The theoretical output from $\mathbf{M}_{PG}$, using an unpolarized input, is fit to the measured output from the microbolometer, using the free parameters in $\mathbf{M}_{PG}$. Performing this least squares fitting operation yields $\delta_{WP} = 76.2º$ and diattenuation coefficient $D_{WP} = 0.031$. This experiment was also preformed to measure the retardance (δ_{WPA}) and diattenuation (D_{WPA}) of the analyzing form-birefringent WP used inside the instrument for measurements of S_3. Measurement of this component yielded $\delta_{WPA} = 85.79º$ and diattenuation $D_{WPA} = -0.0693$.

3.6 S_1, S_2 and S_3 calibration

The PG setup for calibrating the polarimeter's S_1 and S_2 measurement configurations, corresponding to WGBS reflection axis orientations of 0º and -45º, respectively, consisted of the linear polarizer at 67.5º followed by the rotating form birefringent WP. This makes the Stokes vector for the PG output,

$$\mathbf{S}_{PG} = \mathbf{M}_R\left(76.2°, \theta_G\right) \cdot \mathbf{M}_D\left(0.031, 0.5, \theta_G\right) \cdot \mathbf{M}_D\left(0.98, 0.1, 67.5°\right) \cdot \begin{bmatrix} 1 & 0 & 0 & 0 \end{bmatrix}^T \tag{15}$$

For the S_1 and S_2 measurement configurations, the Mueller matrices take the form,

$$\mathbf{M}_T^{S_1} = \mathbf{M}_D\left(D_T^{S_1}, E_T^{S_1}, \theta_T^{S_1}\right) \cdot \mathbf{M}_R\left(\delta_{AR,T}^{S_1}, \theta_{AR,T}^{S_1}\right) \tag{16}$$

$$\mathbf{M}_R^{S_1} = \mathbf{M}_D\left(D_R^{S_1}, E_R^{S_1}, \theta_R^{S_1}\right) \cdot \mathbf{M}_R\left(\delta_{AR,R}^{S_1}, \theta_{AR,R}^{S_1}\right) \tag{17}$$

$$\mathbf{M}_T^{S_2} = \mathbf{M}_D\left(D_T^{S_2}, E_T^{S_2}, \theta_T^{S_2}\right) \cdot \mathbf{M}_R\left(\delta_{AR,T}^{S_2}, \theta_{AR,T}^{S_2}\right) \tag{18}$$

$$\mathbf{M}_R^{S_2} = \mathbf{M}_D\left(D_R^{S_2}, E_R^{S_2}, \theta_R^{S_2}\right) \cdot \mathbf{M}_R\left(\delta_{AR,R}^{S_2}, \theta_{AR,R}^{S_2}\right) \tag{19}$$

where the superscripts denote the measurement configuration (S_1 or S_2), subscripts T or R indicate transmission or reflection, respectively, δ_{AR} is the retardance of the thin-film AR coating on the WGBS, θ_{AR} is the orientation of the thin film's retardance with respect to the x-axis, θ_T and θ_R are the orientations of the WGBS transmission or reflection axes, respectively, and D_T, D_R, E_T, and E_R are the diattenuation coefficients for reflection and transmission. Retardance is inherent in thin-film AR coatings at non-normal incidence angles. It is bound to the plane of incidence and is due to the change in the characteristic admittance of the coating for s and p polarizations [10, 11]. Consequently, the retardance in the WGBS's AR coating is modeled using the Mueller matrix of a general retarder.

For measurements of S_3, the analyzing WP is inserted into the optical path and the WGBS is oriented with its reflection axis at 0º. The Mueller matrices for transmission and reflection take the form,

$$\mathbf{M}_T^{S_3} = \mathbf{M}_T^{S_1} \cdot \mathbf{M}_D\left(D_{WPA,T}, 0.5, \theta_{WPA,T}\right) \cdot \mathbf{M}_R\left(\delta_{WPA,T}, \theta_{WPA,T}\right) \tag{20}$$

$$\mathbf{M}_R^{S_3} = \mathbf{M}_R^{S_1} \cdot \mathbf{M}_D\left(D_{WPA,R}, 0.5, \theta_{WPA,R}\right) \cdot \mathbf{M}_R\left(\delta_{WPA,R}, \theta_{WPA,R}\right) \tag{21}$$

where θ_{WPA} is the orientation, D_{WPA} is the diattenuation, and δ_{WPA} is the retardance of the analyzing WP. Again the value of E in $\mathbf{M}_D$ for the WP is set to 0.5; this is valid given the small diattenuation ($D < 0.1$) in the wave plate. Results of the fitting procedure are presented in Fig. 5, where the measured reflected and transmitted generator response for the center (on-axis) pixel is plotted along side the fitted curve for the S_1, S_2 and S_3 analyzer configurations.

3.7 Calibration refinement

In order to further refine the reduction matrices, data were taken of the PG in the following configurations to achieve an adequate sampling of the Poincaré sphere [7],

1. Linear polarizer at 0º followed by a rotating WP.
2. Linear polarizer at 67.5º followed by a rotating WP.
3. Rotating linear polarizer.

Measurements of each PG configuration were achieved at both high and low black body temperatures for each field position. All rotations were preformed in 20º increments from 0º to 360º. Unlike the previous fitting procedures, where variables in the Mueller matrices (e.g. diattenuation, orientation and retardance) were used as degrees of freedom for the fitting, refinement here focuses on adjusting the measurement matrix components directly to achieve the fit. In order to refine the reduction matrix, the theoretical Stokes vector output of the PG was calculated and compared to the reconstructed output using the measured reduction matrices.

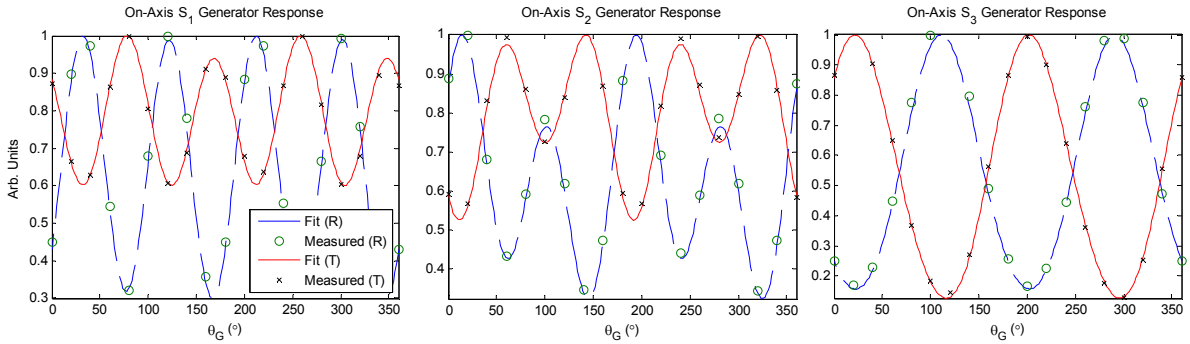

(a) (b) (c)

Fig. 5. On-axis fit of the polarimeter's S_1 (a), S_2 (b), and S_3 (c) response to the PG input. The measured data are presented alongside the fitted results for reflection (R) and transmission (T).

The coefficients from the previous fitting procedure were used as a starting point to guide the optimization. A merit function (ε) was constructed that used the root mean square difference between the measured and theoretical output for each Stokes parameter,

$$\varepsilon = \sqrt{\frac{1}{N}\sum_{n=1}^{N}\left[\eta_1\left(S_1(n)-S_{1,PG}(n)\right)^2+\eta_2\left(S_2(n)-S_{2,PG}(n)\right)^2+\eta_3\left(S_3(n)-S_{3,PG}(n)\right)^2\right]} \tag{22}$$

where η_1, η_2, and η_3 are weighting coefficients and N is the total number of measurements related to θ_G. For our optimization, η_1, η_2, and η_3 are 1.0, 1.0, and 0.1, respectively, where a lower weighting was placed on the circular component due to the broadband nature of the polarimeter.

Optimization was accomplished by adjusting each coefficient in **W** by a small constant (+/- ν), and the most optimal change after each cycle was maintained and carried on to the next cycle. Adjustment of **W** was repeated until the merit function was minimized. To demonstrate the level of improvement, the RMS error of all PG configurations (1-3) for each Stokes parameter before and after optimization are calculated by,

$$\varepsilon_{S_i,pre/post} = \sqrt{\frac{1}{N}\sum_{n=1}^{N}\left(S_i(n)-S_{i,pre/post}(n)\right)^2} \tag{23}$$

where the subscript *pre* or *post* indicates pre or post optimization, respectively, and *i* is an integer that indicates the Stokes parameter being analyzed. This yields pre and post on-axis optimization S_1 errors of $\varepsilon_{S_1,pre}=0.0580$ and $\varepsilon_{S_1,post}=0.0131$, S_2 errors of $\varepsilon_{S_2,pre}=0.0898$ and $\varepsilon_{S_2,post}=0.0255$, and S_3 errors of $\varepsilon_{S_3,pre}=0.0732$ and $\varepsilon_{S_3,post}=0.0229$, demonstrating that optimization decreases the RMS error by at least a factor of 3 for all cases. Since this is a comparison of the error before and after the fitting procedure, it is naturally anticipated that any error metric will yield improved postoptimization errors. Therefore, further validation of the calibration refinement technique, by use of different polarization generators than were used in the calibration, was accomplished. Results from this are presented in Ref. [8].

4.0 RESULTS

In order to demonstrate the effectiveness of the sensor, a variety of indoor and outdoor tests were preformed. These included observations of a smooth spherical emitter, outdoor vehicles, and vehicles imaged from a moving platform.

4.1 Spherical emitter

An important laboratory test used to verify the calibration consisted of imaging a solid 125 mm diameter obsidian glass sphere that was heated uniformly in warm water to 34 ºC and imaged under a shroud with a background temperature of 20.4 ºC. An image of the experimental setup is provided in Fig. 6.

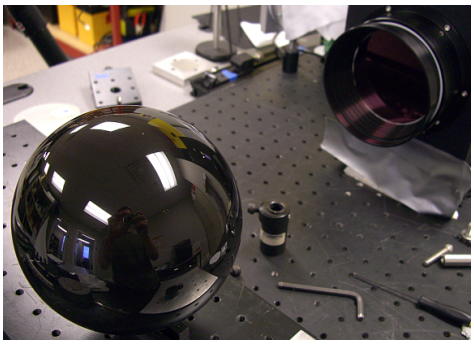

Fig. 6. Obsidian glass sphere experimental setup with shroud removed in front of the polarimeter.

Consecutive measurements for all three states were acquired, yielding the four Stokes parameter images in Fig. 7. Combining these data through the use of a color-fusion technique yields the images in Fig. 8 [12]. In color-fusion, a hue-saturation-value (HSV) color mapping scheme is used in which the orientation of the polarization ellipse, the degree of linear polarization (DOLP) and the intensity image (S_0) are used as the hue, saturation, and value, respectively.

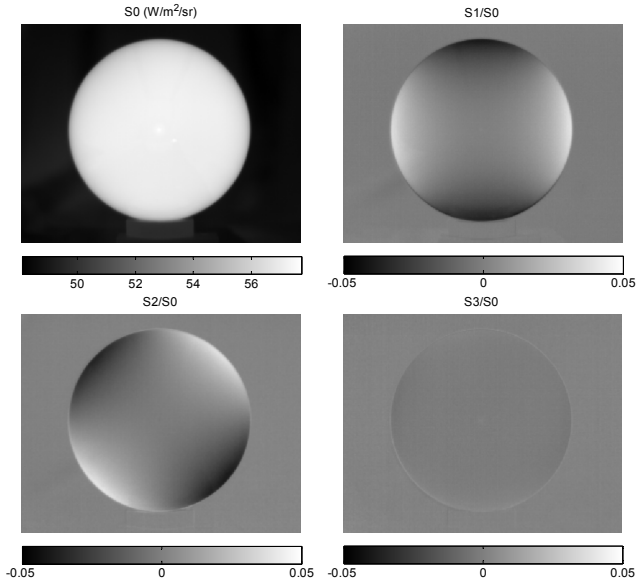

Fig. 7. Stokes parameter images of the obsidian glass sphere.

The DOLP and its orientation, θ_L, are calculated from S_1 and S_2 in Fig. 7 by [13],

$$DOLP(m,n) = \frac{\sqrt{S_1(m,n)^2 + S_2(m,n)^2}}{S_0(m,n)} \tag{24}$$

$$\theta_L(m,n) = \frac{1}{2}\tan^{-1}\left(\frac{S_2(m,n)}{S_1(m,n)}\right) \tag{25}$$

For our images magenta, red, yellow, green, cyan, and blue represent linear polarization orientations of 0º, 30º, 60º, 90º, 120º, and 150º, respectively. A similar approach can be used for the circular component, where the handedness (the sign on S_3), degree of circular polarization (DOCP) and the intensity image (S_0) are used as the hue, saturation and value, respectively.

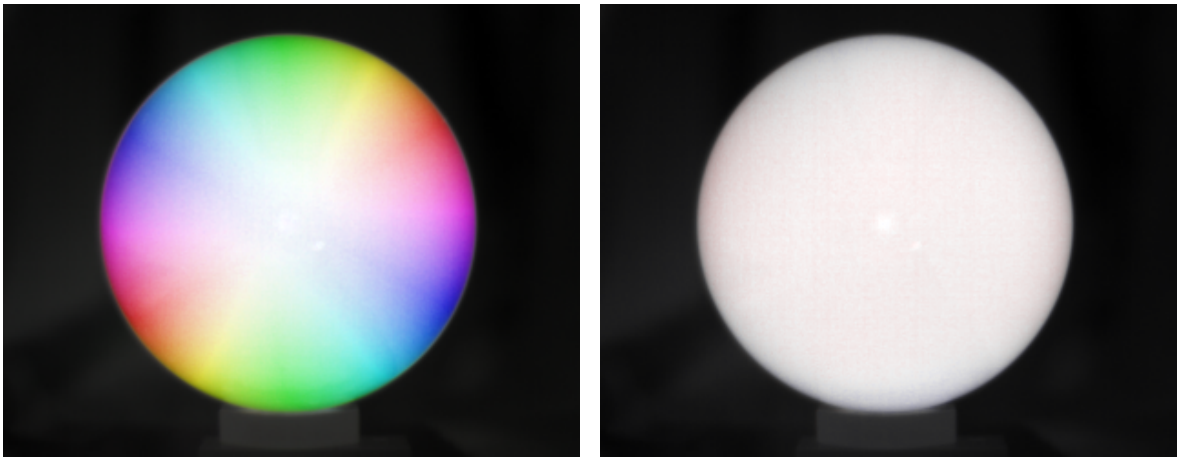

(a) (b)

Fig. 8. (a) Color-fusion image of DOLP (saturation), orientation (hue), and intensity (grayscale value) for the obsidian glass sphere. (b) Color-fusion image of the DOCP (saturation), handedness (hue), and intensity (grayscale value). Full saturation occurs at a DOLP or DOCP of 0.05.

The DOCP is calculated as,

$$DOCP(m,n) = \left| \frac{S_3(m,n)}{S_0(m,n)} \right| \tag{26}$$

Since the sign of S_3 determines the color, only two colors are used for the DOCP color-fusion image. In our case, red and blue indicate left and right circular handedness, respectively, while gray indicates no circular component is present. It should be noted that in Fig. 8 little color is present, which is indicative of minimal circular polarization.

To verify these results, the complex index of refraction for bulk obsidian per Ref. [14] was calculated to have a band-averaged value over 7.5 - 13.5 μm of (n, k) ~ (1.6, 0.47). Calculating the anticipated DOLP output of the sphere, in a radial cross-section, is portrayed in Fig. 9. The theoretical and measured values for the DOLP agree with each other to within 0.23% RMS. For the DOCP component no theoretical S_3 output is present, which again is observed in Fig. 8 (b) by the absence of color. The agreement between the theoretical and measured DOCP is similar to the DOLP with a value of 0.15% RMS.

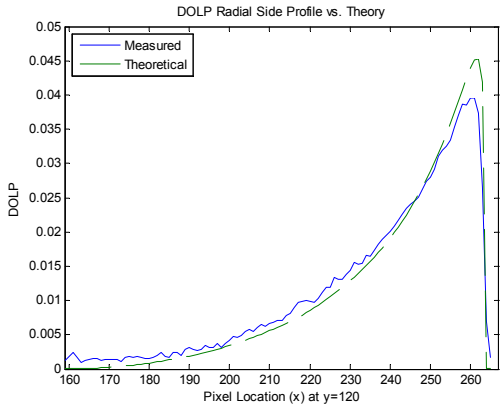

Fig. 9. Radial cross-section of the DOLP from the sphere; measured and theoretical versus pixel location.

4.2 Outdoor vehicles

Other objects were observed during outdoor testing. Fig. 10 illustrates DOLP and DOCP color-fusion images of a parking lot under mostly clear skies.

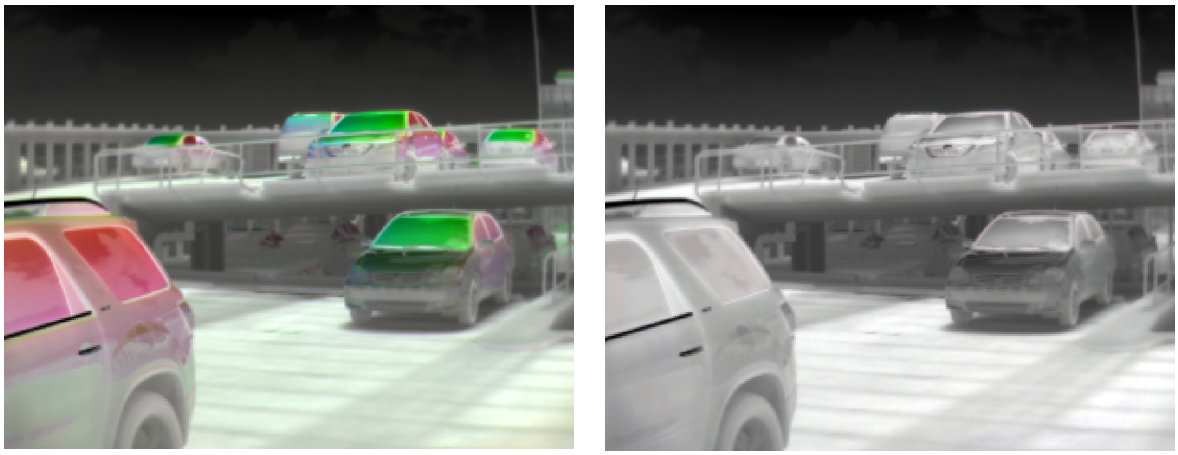

(a) (b)

Fig. 10. Color-fusion images of (a) DOLP and (b) DOCP on top of a parking garage on a clear day. Full saturation occurs at a DOLP or DOCP of 0.12 and is approximately the maximum DOLP present in (a).

From this scene, it is apparent that little circular polarization is present. Reasons behind this primarily involve the fact that S_3 is generally observed in reflections off surfaces given an incident field that is already linearly polarized. Consequently, the small S_3 signatures that do appear are likely due to residual miscalibration, causing cross-talk between the linearly and circularly polarized signals during data reduction.

4.3 Moving platform data

Previous data showed completely stationary targets. When the scene or platform is moving, the sensor must operate in S_1, S_2 or S_3. From our experiments, we have concluded that the largest signal is located when one views in S_1 for most target geometries (assuming that the polarimeter is oriented horizontally). Data captured while the sensor was moving on top of a vehicle is depicted in Fig. 11. Polarization errors due to platform motion are negligible for these data since the system is collecting the two measurements needed for S_1 simultaneously.

(a) (b)

Fig. 11. (a) Color-fusion of an S_1 Stokes parameter image taken from a moving vehicle that was driving past a pickup truck. (b) Intensity image (S_0). Full color saturation occurs at a value of 0.06. Red and blue denote vertical and horizontal polarizations, respectively.

5.0 CONCLUSION

Validity of the calibration procedure was established by comparison of the recorded measurement matrix to that of the band-averaged matrix obtained from theoretical RCWA calculations. Comparison between these values over the FOV yielded an average RMS error of 3.4%, 4.2% and 8.2% for the S_1, S_2 and S_3 measurement configurations, respectively. Remaining error, especially in the case of S_3, can be attributable to the non-achromatic spectral response of the instrument. Regardless of these errors, which can only be remedied by spectrally resolving the measurements, the system still performs admirably as a broadband infrared polarimeter. Demonstration of this was provided by comparison of a solid obsidian glass sphere's emission to theory, in which RMS errors are 0.23% and 0.15% for DOLP and DOCP values, respectively.

A two-camera imaging Stokes polarimeter based on uncooled microbolometer detectors has been demonstrated to produce reliable polarimetric data. By using microbolometers, a polarimeter with reduced cost over an MCT-based sensor can be realized. Additionally, a lack of cryogenically cooled components makes such an instrument viable in applications requiring near instantaneous startup of the imager, while also contributing to the system's reduced footprint, weight and power consumption. Future work includes investigations into scene-based non-uniformity corrections and further study of how the non-achromatic nature of the sensor influences the measured Stokes parameters.

REFERENCES

1. J. S. Tyo, D. L. Goldstein, D. B. Chenault, and J. A. Shaw, "Review of passive imaging polarimetry for remote sensing applications," *Appl. Opt*. **45** (22), 5453-5469 (2006).
2. M. W. Kudenov, J. L. Pezzaniti, E. L. Dereniak and G. R. Gerhart, "2-Cam LWIR Imaging Stokes Polarimeter" *Proc. of SPIE*. **6972**, 697220K (2008).
3. L B. Wolff. "Polarization camera for computer vision with a beam splitter," *J. Opt. Soc. Am*. **11** (11), 2935-2945 (1994).
4. J. A. Shaw, P. W. Nugent, N. J. Pust, and B. Thurairajah. "Radiometric cloud imaging with an uncooled microbolometer thermal infrared camera," *Opt. Exp*. **13** (15), 5807-5817 (2005).
5. C. Persons, M. Jones, C. Farlow, L. Morell et. al. "A proposed standard method for polarimetric calibration and calibration verification," Proc. of SPIE. **6682**, 66820K (2007).
6. J. L. Pezzaniti and D. B. Chenault. "A Division of Aperture MWIR Imaging Polarimeter," *Proc. of SPIE*. 5888, 58880V (2005).
7. D. L. Goldstein. Polarized Light, Marcel Dekker Inc., New York (2003).
8. M. W. Kudenov, J. L. Pezzaniti, E. L. Dereniak and G. R. Gerhart, "Microbolometer infrared imaging Stokes polarimeter," *Opt. Engr*., **48** (6), (2009).
9. R. R. Boye, S. A. Kemme, J. R. Wendt, A. A. Cruz-Cabrera, and G. A. Vawter. "Fabrication and measurement of wideband achromatic waveplates for the mid-infrared using subwavelength features," *J. Microlith., Microfab., Microsyst*., **5** (4), 043007 (2006).
10. J. P. McGuire Jr., R. A. Chipman. "Polarization aberrations. 1. Rotationally symmetric optical systems," *Appl. Opt*. **33** (22), 5080-5100 (1994).
11. H. A. Macleod, Thin-film optical filters, p. 20, A. Higler Ltd., London (1969).
12. J. S. Tyo, E. N. Pugh, and N. Engheta, "Colorimetric representations for use with polarization-difference imaging of objects in scattering media," *J. Opt. Soc. Am*., **15**, 367-374 (1998).
13. R. M. A. Azzam and N. M. Bashara. Ellipsometry and Polarized Light, pp. 51, North-Holland, Amsterdam (1988).
14. C. Koike, H. Hasegawa, N. Asada, and T. Komatuzaki. "Optical constants of fine particles for the infrared region," *Mon. Not. R. Astr. Soc*. **239**, 127-137 (1989).